Propagation-based X-ray phase-contrast tomography of mastectomy samples using synchrotron radiation

T. E. Gureyev[1,2,3,4,a], Ya. I. Nesterets[4,5], P. M. Baran[1], S. T. Taba[2], S. C. Mayo[5], D. Thompson[4,5], B. Arhatari[1,6], A. Mihocic[6], B. Abbey[6], D. Lockie[7], J. Fox[3], B. Kumar[3], Z. Prodanovic[3], D. Hausermann[8], A. Maksimenko[8], C. Hall[8], A. G. Peele[8], M. Dimmock[3], K. M. Pavlov[9,3,4], M. Cholewa[10], S. Lewis[2], G. Tromba[11], H. M. Quiney[1] and P. C. Brennan[2]

[1] The University of Melbourne, Parkville 3010, Australia
[2] The University of Sydney, Lidcombe 2141, Australia
[3] Monash University, Clayton 3800, Australia
[4] University of New England, Armidale 2351, Australia
[5] Commonwealth Scientific and Industrial Research Organisation, Clayton 3168, Australia
[6] La Trobe University, Bundoora 3086, Australia
[7] Maroondah BreastScreen, Ringwood East 3135, Australia
[8] Australian Synchrotron, ANSTO, Clayton 3168, Australia
[9] University of Canterbury, Christchurch 8041, New Zealand
[10] University of Rzeszow, 35-310 Rzeszow, Poland
[11] Elettra Sincrotrone, 34149 Basovizza, Trieste, Italy
[a] Author to whom correspondence should be addressed. Electronic mail: timur.gureyev@unimelb.edu.au; Telephone: (+61) 3-834-47497.

Purpose: Propagation-based phase-contrast computed tomography (PB-CT) is a method for three-dimensional X-ray imaging that utilizes refraction, as well as absorption, of X-rays in the tissues to increase the signal-to-noise ratio (SNR) in the resultant images, in comparison with equivalent conventional absorption-only X-ray tomography (CT). Importantly, the higher SNR is achieved without sacrificing spatial resolution or increasing the radiation dose

29   delivered to the imaged tissues. The present work has been carried out in the context of the

30   current development of a breast CT imaging facility at the Australian Synchrotron.

31   **Methods:** Seven unfixed complete mastectomy samples with and without breast cancer

32   lesions have been imaged using absorption-only CT and PB-CT techniques under controlled

33   experimental conditions. The radiation doses delivered to the mastectomy samples during the

34   scans were comparable to those approved for mammographic screening. Physical

35   characteristics of the reconstructed images, such as spatial resolution and SNR, have been

36   measured and compared with the results of the radiological quality assessment of the

37   complete absorption CT and PB-CT image stacks.

38   **Results:** Despite the presence of some image artefacts, the PB-CT images have outperformed

39   comparable absorption CT images collected at the same radiation dose, in terms of both the

40   measured objective image characteristics and the radiological image scores. The outcomes of

41   these experiments are shown to be consistent with predictions of the theory of PB-CT

42   imaging and previous reported experimental studies of this imaging modality.

43   **Conclusions:** The results presented in this paper demonstrate that PB-CT holds a high

44   potential for improving on the quality and diagnostic value of images obtained using existing

45   medical X-ray technologies, such as mammography and digital breast tomosynthesis (DBT).

46   If implemented at suitable synchrotron imaging facilities, PB-CT can be used to complement

47   existing imaging modalities, leading to more accurate breast cancer diagnosis.

48

49   **1. INTRODUCTION**

50

51   Breast cancer is the leading cause of cancer fatalities for women [1]. Despite some recent

52   controversy about the efficacy of the procedure, regular mammographic screening is

53   recommended by health authorities in most developed countries as an optimal strategy for

54   detecting the first signs of breast cancer, since early detection is crucial for successful

55   treatment of this common type of cancer, before it spreads to vital organs [2]. Even though

56   considerable progress in the development of alternative methods for breast imaging

57   (ultrasound, magnetic resonance imaging (MRI), terahertz radiation, photoacoustic

58   tomography and others) has been achieved in recent years, X-ray mammography remains the

59   mainstream method for mass breast screening. Notwithstanding a considerable improvement

60   in the performance of X-ray mammographic systems in recent years, the technique still

61   demonstrates relatively high rates of both false negatives and false positive diagnoses.

62   According to the National Cancer Institute, mammography misses about 20% of cancers [2],

63 indicating that the potential for better performance of X-ray mammography is still high.

64 There remains a considerable incentive for the development of improved mammographic

65 techniques which would lead to a reduction in false positives and false negatives diagnoses,

66 deliver reduced X-ray dose to the patient and, preferably, would also reduce or remove

67 physical discomfort experienced by many patients during conventional breast screening

68 procedures [3-11].

69   Among the newer techniques, digital breast tomosynthesis (DBT) has become the

70 leading approach to 3D mammography. Publications (including recent studies performed by

71 members of our team) confirm that X-ray DBT is capable of an improvement in the

72 sensitivity and specificity of breast cancer diagnosis compared to conventional 2D

73 mammography [12,13]. Sensitivity and specificity still remain, however, below optimal

74 levels. It is well-accepted that computed tomography (CT) is generally superior to DBT in

75 terms of the fidelity of 3D reconstruction, but radiation dose with CT is a major issue. If the

76 dose could be kept at a level comparable with that in the present-day clinical 2D two-view

77 mammography or DBT, while ensuring sufficient spatial resolution and signal-to-noise ratio

78 (SNR), mammographic CT could outperform all other X-ray imaging techniques. In this

79 context, phase-contrast X-ray CT, which utilises refraction as well as absorption, of X-rays in

80 tissue, shows particular promise due to its superior sensitivity to soft-tissue tumours. This

81 enables better-quality images to be obtained at lower radiation doses compared to

82 conventional absorption-based CT [6,7,9,14,15,16].

83   Up to 76% of women experience pain or discomfort during a mammographic

84 procedure with moderate levels of pain persisting for up to four days post-examination [17].

85 A recent Cochrane review demonstrated that current interventions had not effectively reduced

86 pain and that further innovations are still required [18]. Since CT imaging does not rely on

87 the uniformity of breast tissue thickness, strong compression is not required with that

88 technique [19]. The reduction in physical discomfort associated with the procedure,

89 combined with the reduced radiation dose in phase-contrast CT, has the potential to increase

90 the participation rate of women in regular breast screening. This would most likely deliver

91 improvements in early cancer detection leading to more successful treatment and, ultimately,

92 decrease the mortality and morbidity associated with breast cancer.

93   In recent years, several different modalities of phase-contrast CT have been studied in

94 conjunction with breast imaging. The main modalities are the propagation-based (also known

95 as in-line) CT (PB-CT) [20], edge illumination CT [21], grating-based CT [22] and analyser-

96 based CT [8,23]. Among these techniques, only PB-CT does not require any specialized X-

97 ray optical elements in order to render the phase-contrast visible. As a consequence, this

98 technique is the easiest to implement in principle, although it requires a highly spatially

99 coherent X-ray illumination to work effectively [24,25]. Therefore, PB-CT is typically

100 implemented either with highly-parallel X-ray beams at synchrotron facilities or with

101 microfocus laboratory X-ray sources that produce quasi-spherical incident X-ray waves. The

102 microfocus X-ray source technology is currently at a stage where it still cannot deliver X-ray

103 illumination of sufficient spatial coherence with a brightness (X-ray flux) that would enable

104 CT scans of a full human breast within a clinically acceptable time. Recent work on the

105 development of PB-CT technology for breast cancer imaging of live human patients has been

106 concentrated at synchrotron facilities [26], especially at Elettra synchrotron in Trieste, Italy

107 [27] and at the Australian Synchrotron in Melbourne [20,28]. In the present paper, we

108 describe some of the latest results obtained in the process of development of breast PB-CT

109 imaging facility at the Imaging and Medical Beamline (IMBL) of the Australian Synchrotron

110 [29,30].

111

112

113 **2. MATERIALS AND METHODS**

114

115 **2.A. Experimental setup**

116

117 The experiments described in the present paper have been carried out at the Imaging

118 and Medical beamline (IMBL) of the Australian Synchrotron (Clayton, Victoria, Australia).

119 This beamline is based on a super-conducting wiggler and provides a wide monochromatic

120 and nearly parallel X-ray beam with an area of up to 500 mm × 40 mm (h×v) at a distance of

121 140 m from the source, at 30 keV energy [29]. A bent double-crystal monochromator is used

122 in the double-Laue configuration to deliver an X-ray beam in an energy range between 20

123 keV and 120 keV (we have used the X-ray energy of 32 keV in this study) with an energy

124 resolution of $\Delta E/E = 10^{-3}$. The X-ray detector used for the present study was a Hamamatsu

125 CMOS Flat Panel Sensor C9252DK-14, utilized in partial scan mode, with pixel size 100 μm

126 × 100 μm, 2432 × 100 pixels (horizontal × vertical) field of view, 12-bit output and typical

127 resolution of 4.5 lp/mm (at CTF=5%).

128 For the CT scans, the mastectomy samples were placed in a thin-walled plastic

129 container, with the nipple area of the breast located near the top. The cylindrical container

130   with the sample inside was then positioned on a rotation stage for CT scans which consisted

131   of 1800 projections each, collected over 180 degrees with the angular step of 0.1 degree.

132   Such an angular step is slightly finer (providing some degree of angular over-sampling) than

133   that corresponding to the optimal Nyquist sampling condition for a CT scan with the 2432

134   detector pixels in each image row [31].

135   The PB-CT scans analysed in this paper were collected at two different sample-to-

136   detector distances. The "short" distance of 0.2 m (or 0.7 m in some cases - see details below)

137   represented the minimum practically achievable distance between the sample and the

138   detector, while the "long" distance of approximately 6 m represented the maximum

139   achievable distance. The images collected at the "short" propagation distance were intended

140   to approximate the conventional absorption-only CT, while the scans at the "long" distance

141   allowed us to maximize the gain in reconstructed image quality due to in-line phase-contrast

142   effects (see details in Section 3.A below).

143   The radiation dose delivered to the sample was monitored during each scan with the

144   help of an ionization chamber, with the subsequent calculations of the mean absorbed dose

145   (MAD) taking into account the size of the sample and using the method described in

146   [15,28,32]. The images described in the present paper were selected from the scans collected

147   at two different dose levels: one approximately equal to 4.5 mGy MAD, which is referred to

148   as "std" dose below, and another one close to 2.3 mGy MAD, referred to as "low" dose, for a

149   complete CT scan (see details in Table 1).

150   The final implementation of the setup for breast PB-CT imaging at IMBL will include

151   an evacuated pipe between the irradiated breast and the X-ray detector, but such a pipe was

152   not installed during the experiments described in the present paper. As a result, the images

153   collected at the sample-to-detector distance of 6 m were negatively affected by X-ray

154   absorption in air, which resulted in a reduction factor of approximately 0.8 (at 32 keV) in the

155   X-ray flux reaching the detector. For example, the X-ray dose of 4.5 mGy used in a PB-CT

156   scan with 6 m propagation distance was equivalent, in terms of the photon statistics in the

157   detector plane, to a dose of $4.5 \times 0.8 = 3.6$ mGy in a similar scan performed at 0.2 m

158   propagation distance, while the dose of 2.4 mGy at 6 m was equivalent to $2.4 \times 0.8 = 1.9$

159   mGy at 0.2 m. In this sense, "std" doses used in our experiment for the scans at the "long"

160   and "short" propagation distances were approximately equivalent, while the "low" dose used

161   with the scans at the "long" distance was effectively approximately 1.7 times lower than the

162   "std" dose at the "short" distances (3.3 mGy / 1.9 mGy $\cong$ 1.7, see Table 1).

163   The standard measure of radiation exposure in breast imaging is mean glandular dose

164   (MGD), however its accurate evaluation requires the knowledge of breast glandularity. In this

165   work we measured the air kerma directly and calculated the mean absorbed dose (MAD)

166   following the approach used previously in [15,28,32] and elsewhere, which assumes 50%

167   mixture of glandular and adipose tissue in the breast sample. Both MAD and MGD are

168   proportional to air kerma, but the two could differ by as much as 25% in certain cases. For

169   the purpose of the present study, the exact value of the radiation dose delivered to the sample

170   was not critical, as the reference and the test images in each comparison pair were collected

171   at the same effective air kerma, and hence with the same MGD, as well as MAD. This allows

172   us to objectively estimate the advantage in the image quality achieved in PB-CT imaging,

173   compared to absorption CT images collected at the same absorbed dose.

174

175

176   **2.B. Breast tissue samples**

177

178   Seven complete unfixed mastectomy samples have been used in this study. The main

179   relevant characteristics of the samples and the key X-ray scan parameters are summarized in

180   Table 1.

181

182   **2.C. CT reconstruction**

183

184   Each collected CT scan effectively comprised 1800 "full-height" projections, as well

185   as 200 "dark-current" images (X-rays off) and 200 "flat-field" images (X-rays on, no sample

186   in the beam). Half of the flat-field and dark-current images were collected immediately

187   before the sample scan, with the other half collected immediately after the sample scan, in

188   order to compensate for the possible temporal variation of the incident beam intensity. Each

189   "full-height" projection was assembled by "stitching" partial projections which had a height

190   of 10 mm and overlap of 2 mm at each common horizontal edge. For example, in order to

191   obtain a single CT scan of a sample with a height of 60 mm, seven or eight sub-scans with a

192   vertical size of 10 mm had to be collected and subsequently stitched. A sample projection

193   from a single sub-scan and a corresponding flat-field and dark-current corrected full-height

194   stitched projection are shown in Fig. 1.

195   The full-height projections, corrected for flat and dark fields, were then used as input

196   to the Homogeneous Transport-of-Intensity equation (TIE-Hom) "phase" retrieval method

197   (also known as Paganin's method) [33,34]. The mathematical procedure corresponding to this

198   method represents an image convolution operation:

199

200   $$I_{ret}(x,y) = \int P_\sigma(x-x', y-y') I_R(x',y')\, dx'dy' \;, \tag{1}$$

201

202   where $I_R(x,y)$ is the intensity distribution of a projection collected at the sample-to-detector

203   distance R, which is a function of Cartesian coordinates (x,y) in the object plane (in a

204   corresponding discrete representation of an image, this intensity is a function of pixel indices

205   (i,j)), $I_{ret}(x,y)$ is the TIE-Hom retrieved image intensity distribution, as a function of

206   Cartesian coordinates in the object plane, and $P_\sigma(x,y)$ is the TIE-Hom point-spread function

207   (PSF). The latter PSF is equal to

208

209   $$P_\sigma(x,y) = (2\pi\sigma^2)^{-1} K_0[\sigma^{-1}(x^2+y^2)^{1/2}], \tag{2}$$

210

211   where K_0 is the zero-order modified Bessel function of the second kind. This PSF represents a

212   low-pass filter, because $K_0(0) = +\infty$, it decreases exponentially, $K_0(z) \sim [\pi/(2z)]^{1/2}\exp(-z)$,

213   when $z \to +\infty$, and $\sigma = \frac{1}{2}(\gamma\lambda R/\pi)^{1/2}$ represents the standard deviation of the PSF (the

214   integral of this PSF is equal to 1, as expected) [35]. It is also well known that the Fourier

215   transform of this PSF is equal to $\hat{P}_\sigma(u,v) = 1/[1 + \pi\lambda\gamma z(u^2+v^2)]$ [33, 35]. It can be seen that

216   the width of this PSF is proportional to the square root of the product of the sample-to-

217   detector distance R, the X-ray wavelength λ and the ratio $\gamma = \delta(\mathbf{r})/\beta(\mathbf{r})$ of the real to

218   imaginary part of the sample's complex refractive index $n(\mathbf{r}) = 1 - \delta(\mathbf{r}) + i\beta(\mathbf{r})$, where

219   $\mathbf{r} = (x,y,z)$ denotes a position inside the sample [35]. Even though in the original theory of

220   TIE-Hom reconstruction [33], the value of γ was assumed to be the same at any point inside

221   the sample, the method described by equations (1)-(2) can in principle be applied to any

222   image, always resulting in an increase of signal-to-noise ratio (SNR), simply because this

223   method represents a low-pass filtering operation. However, if γ varies across the sample, as

224   is generally the case for breast tissues, the application of the TIE-Hom method with

225   $\gamma = \text{constant}$ (as in the present study) to a propagated image may result in incomplete

226   compensation of phase-contrast effects in some areas and excessive blurring in other areas.

227 As these effects have been studied and explained in detail elsewhere [28,36], we will not

228 discuss them further here.

229 It has been shown [35] that the application of the TIE-Hom retrieval method, in the

230 form described by eqs.(1)-(2), to CT projections collected at a sample-to-detector distance R,

231 followed by conventional filtered back-projection (FBP) CT reconstruction, leads to a gain in

232 SNR in the reconstructed CT slices, compared to the SNR in the corresponding CT slices

233 reconstructed without phase retrieval from contact ($R = 0$) projections collected at the same

234 X-ray dose. The gain coefficient is approximately equal to

235

236 $$G \equiv \frac{SNR_{ret}}{SNR_{contact}} \approx 0.28 \, A \left(\frac{T_R}{\ln A - 1} \right)^{1/2}, \tag{3}$$

237

238 where $A \equiv (\pi/4)\gamma\lambda R / h^2$, h is the detector pixel size and T_R is the transmittance of X-rays in

239 the gap between the sample and detector [35]. Equation (3) is valid under the following

240 assumptions: 1) the modulation transfer function of the detector is equal to one (i.e. there are

241 no correlation of noise in raw projections), 2) the dimensionless parameter A is much greater

242 than one, 3) nearest neighbor interpolation is used in the FBP algorithm, and 4) ramp filter is

243 used in the CT reconstruction from phase-contrast projections, while Hann filter is used in the

244 reconstruction from contact projections. It can be easily verified that, under the conditions

245 employed in the present experiments, i.e. with $\gamma = 550$ representing the relative ratio

246 $(\delta_g - \delta_b)/(\beta_g - \beta_b)$ of glandular breast tissue (g) and blood (b) at the X-ray energy of 32

247 keV, $\lambda = 0.039$ nm, $R = 6$ m and $h = 100$ μm, one obtains $\sigma = 101.20$ μm and $G \cong 2.17$. The

248 estimated gain factor reduces if one takes into account the finite resolution of the detector and

249 uses linear interpolation in the FBP algorithm. Other experimental imperfections can also

250 affect these estimates. In the end, we have not observed a gain factor larger than 1.76 in our

251 experimental images (see Table 2). However, some of the "technical" detrimental

252 experimental factors can be removed or reduced in a future implementation of PB-CT breast

253 imaging, leading to larger values of the gain factor. For example, if an X-ray detector with a

254 pixel size of 50 μm is utilized, it would push the gain factor to $G = 6.06$ under the same

255 experimental conditions as considered above, increasing further to $G = 6.80$ with the

256 installation of an evacuated pipe between the sample and the detector. Equivalently, the last

257 gain factor can be converted into the reduction of the X-ray dose by a factor of 46 at the same

258 SNR as in the corresponding absorption-only CT images [35].

259   It is also important to keep in mind that considering SNR without a reference to the

260   corresponding spatial resolution in the image is usually meaningless [37]. Indeed, it is often

261   possible to apply a low-pass filter to an image and increase its SNR that way. Such filtering

262   always leads, however, to a commensurate loss of spatial resolution unless *a priori*

263   information about the sample can be utilized in the process. This trade-off between SNR and

264   spatial resolution can be also employed in reverse. Image resolution can often be improved in

265   post-processing by using, for example, a deconvolution operation, but it inevitably amplifies

266   noise and lowers SNR. As a result, a more physically meaningful measure, termed "intrinsic

267   imaging quality characteristics", is represented by a ratio of SNR to spatial resolution,

268   normalized by the square root of the incident photon fluence (number of photons per unit

269   area) F_{in} [37]:

270

271     $$Q = \frac{SNR}{h' F_{in}^{1/2}},$$ (4)

272

273   where h' denotes the spatial resolution of the imaging system (which is equal to h in the

274   "ideal" case of a detector with single-pixel PSF). The quantity Q is invariant with respect to

275   linear image filtering, because SNR increases or decreases in exactly the same proportion as

276   the spatial resolution h' [37]. No form of linear image filtering, including the one described

277   by eq.(1), can increase Q.

278   The PB-CT method, which combines forward free-space propagation of the

279   transmitted coherent X-ray wave from the sample to the detector with "phase" retrieval in

280   accordance with eq.(1), does increase Q, in comparison with that for a contact CT obtained at

281   the same incident fluence (and hence, the same X-ray dose). This increase of Q is only

282   possible because the forward free-space propagation improves spatial resolution (effectively

283   decreasing h') without increasing image noise (see detailed explanation in [38]).

284   Understanding this point is very important in order to appreciate the difference between the

285   PB-CT method employed in the present study and any form of image processing that can be

286   utilized in conjunction with conventional absorption-based CT. While the latter cannot

287   improve SNR in the reconstructed slices without sacrificing the spatial resolution or

288   increasing the X-ray dose, PB-CT is capable of achieving this goal [38], as demonstrated

289   earlier [14,15,16,28] and discussed further below.

290

291   **2.D. Radiological assessment**

292

293   Due to the geometry of our CT scans, the standard FBP-reconstructed CT slices

294   corresponded to the so-called coronal sections (considering the breast attached to the patient's

295   body, i.e. before the mastectomy operation). As it is more conventional for radiologists and

296   pathologists to examine sagittal and axial breast tissue sections instead (which correspond to

297   standard mammographic imaging planes), we re-sliced the reconstructed 3D volumes

298   accordingly. When preparing both the sagittal and the axial slices for analysis, we merged

299   them into 1 mm thick slices (corresponding to the DBT standard) using the Maximum

300   Intensity Projection method, while preserving full original transverse resolution (100 μm

301   pixels) within each slice.

302   The PB-CT ("test") slice stacks were compared with the contact ("reference") slices

303   obtained from CT scans collected with the same sample and same scan conditions (described

304   in the previous section), except for the sample-to-detector distance and the radiation dose. As

305   explained above, the "std" doses were approximately equivalent for the "test" and "reference"

306   scans, while the "low" dose, used only for some of the "test" slices, was about effectively 1.7

307   times lower compared to the "reference" scan. Nine medical imaging specialists and five

308   practicing radiologists (specializing in breast imaging) were asked to look at 14 pairs of "test"

309   and "reference" slice sets, each pair consisting either of "std" dose PB-CT images and "std"

310   dose absorption CT images, or "low" dose PB-CT images and "std" dose absorption CT

311   images. The assessors were asked to compare the pairs of stacks of images and fill in an

312   assessment table according to the following written instructions: "After examining the quality

313   of the stack of images ("Test" images) prepared in axial and sagittal planes, in comparison

314   with the same stacks of "Reference" images, please, nominate a single overall comparative

315   rating for each of the 7 image attributes by putting a cross mark (X) in exactly one cell in

316   each of the attribute rows in the table above. The meaning of the rating scores is as follows:

317   the fulfilment of the corresponding criteria in the test images is clearly better than (+2);

318   slightly better than (+1); equal to (0); slightly worse than (-1); and clearly worse than (-2) the

319   fulfilment of that criteria in the reference images. The intended meaning of image attributes is

320   as follows. Overall quality: overall radiological quality of the image. Perceptible contrast:

321   difference between low and high radiolucency in various soft tissue regions. Lesion

322   sharpness: clarity of definition of lesions and spiculations. Normal tissue interfaces: clarity of

323   visualisation of interfaces between fatty and fibroglandular tissues. Calcification visibility:

324   sharpness of micro-calcifications (if any). Image noise: presence of quantum mottle in the

325   image. Artefacts: evidence of any other technical artefacts such as rings or distortions."

326

327

328   **3. RESULTS**

329

330   Figures 2a and 2b show an example of a slice of sample C1 obtained, respectively,

331   from the "absorption-only" projections collected at $R = 0.2$ m and 3.3 mGy dose, and from

332   PB-CT projections collected at $R = 6$ m at an approximately equivalent dose and

333   reconstructed with the help of eqs.(1)-(2). An improvement of image quality can be observed

334   in the PB-CT image compared to the absorption image. This was confirmed by both

335   "subjective" radiological assessment (+1.75 and +1.33 average scores out of 2.0 maximum,

336   assigned by medical imaging experts and radiologists, respectively, in favor of the PB-CT

337   images), and "objective" measurements of SNR (5.38 vs 9.46, respectively) and spatial

338   resolution (166 μm vs 195 μm, respectively). The "objective" measurements are described in

339   detail in the next section.

340   The results of the radiological assessments, averaged separately across the nine

341   imaging experts ("Experts score") and five radiologists ("Radiol. score"), are presented in

342   the last two columns of Table 2. The order in which the image stack pairs were presented to

343   the assessors was randomized. The correspondence between the sample (case) numbers

344   together with the relevant radiation doses, and the successive image stack pairs, numbered

345   from (Ref_1, Test_1) to (Ref_14, Test_14) according to the order in which these pairs were

346   presented to the assessors, is shown in columns 1 and 2 of Table 2. The scores in the last two

347   columns of Table 2 were obtained by comparing the "test" image against the corresponding

348   "reference" image, as explained above.

349   We have also systematically measured the spatial resolution in two orthogonal

350   directions ("xres" and "yres") of the reconstructed slices corresponding, respectively, to the

351   horizontal and vertical axes of the reconstructed sagittal and axial slices. The SNR and the

352   ratio of the SNR to the average spatial resolution (which corresponded to Q multiplied by the

353   square root of the incident photon fluence) in every tenth sagittal and axial slice of the

354   reconstructed slice stacks have also been measured. The results were then averaged over all

355   analyzed slices (typically, ten per CT slice stack), both sagittal and axial, for a given slice

356   stack. These results can be seen in columns 3-6 of Table 2, with column 7 containing the

357   pair-wise differences between the SNR-to-resolution ratios of the "test" (PB-CT) and
358   "reference" ("absorption" CT) images.

359   Note also that the method for spatial resolution measurement that we applied in this
360   study, as implemented in X-TRACT software [34] and described in detail in [15,36], takes
361   into account the PSF of the detector, but not the X-ray source size. However, under the
362   experimental conditions used in this work, the effect of the X-ray source on the spatial
363   resolution was quite small due to the geometrical demagnification factor, which was
364   approximately equal to 0.0014 for the scans at 0.2 m sample-to-detector distance and 0.041
365   for the scans at 6 m.

366   Figure 3 summarizes the results presented above. It depicts the overall relative image
367   quality scores averaged across nine medical imaging experts and five radiologists, assigned to
368   PB-CT "test" images in comparison with the corresponding "reference" absorption-only CT
369   images, alongside with the differences of the SNR-to-spatial-resolution ratios for the same
370   pairs of test and reference images.

371

372

373   **4. DISCUSSION**

374

375   It can be noticed in Table 2 that the "xres" and "yres" values in the "reference"
376   images were consistently different, equaling to about 2 pixels and 1.4 pixels (i.e. 200 μm and
377   140 μm), respectively, in all reference images. It transpired that this difference was caused by
378   the smoothing effect of the Hahn filter used in the FBP CT reconstruction, which affects only
379   the "horizontal" plane of the original FBP-reconstructed slices [31]. The latter plane
380   corresponds to the coronal plane in the standard medical imaging geometry, and hence affects
381   only the "vertical" ("yres") direction of the sagittal and axial slices. The Hahn filter was not
382   used in the reconstruction of the "test" PB-CT images, because the TIE-Hom filter was
383   applied there instead. The latter filter affects both the horizontal and vertical directions of the
384   original CT projections in equal measure, as can be seen in eqs.(1)-(2), and as a result the
385   "xres" and "yres" values in the resultant PB-CT slices were consistently similar, equaling to
386   about 1.9 pixels (190 μm) in all cases.

387   Some clear trends can be observed also in Fig. 3.
388   (1) All PB-CT images obtained at the same radiation dose as in absorption-only images have
389   received higher scores compared to absorption-only reference CT images. This indicates a

390   clear and consistent advantage achieved by utilizing X-ray phase contrast in the PB-CT

391   method.

392   (2) All PB-CT images, collected at a lower radiation dose, have received lower scores

393   compared to PB-CT images of the same sample collected at a higher radiation dose. Such

394   behavior, of course, was naturally expected.

395   (3) The overall assessed quality of low-dose PB-CT images was on average similar to that of

396   standard-dose absorption-based images (it was better for some samples and worse for the

397   others) (Fig.4). We believe that by improving the implementation of PB-CT method and, in

398   particular, using a better detector, as discussed above, it should be possible in the future to

399   make this result more consistent across different samples.

400   (4) With some exceptions, the general trends were similar between the subjective image

401   quality scores and the differences in SNR-to-spatial-resolution ratios, indicating a correlation

402   between the objective image quality measure (Q) and the results of the subjective image

403   assessment.

404   However, we also observed some "exceptions" to this trend. The most notable

405   "exceptions" among the datapoints in Fig. 3 were represented by the difference between the

406   average SNR/resolution values for the "test" and "reference" images (blue curve) at points

407   number three and nine, i.e. for samples C2 "std" and C5 "std" (see also Table 2).

408   A close re-inspection of these particular sets of CT slices have revealed that the

409   corresponding samples had relatively high glandularity and, as a result, they had relatively

410   few "uniform" image areas of adipose tissue of the size sufficient for reliable, reproducible

411   and representative measurement of SNR. As a consequence, the regions where the SNR

412   measurements have been performed inevitably contained some larger-scale "non-

413   uniformities" represented by inclusions of tumours and glandular tissues, as well as smaller-

414   scale non-uniformities seemingly representing genuine variations in the local density of the

415   fatty tissues. These tissue density variations could not be separated from the true image noise

416   in the measurement of SNR used in this work, which led to artificially lower measured values

417   of SNR in PB-CT slices, compared to the subjective appearance of the images, where the

418   "test" images looked noticeably sharper than the "reference" images. For these reasons, in

419   these two cases in particular, the corresponding relatively high scores given by the imaging

420   specialists and radiologists disagreed with the relatively low values of measured image SNR

421   (see Fig.(5)). In our future studies we plan to investigate this issue further and use other

422   objective image quality metrics, such as, for example, local "visibility", represented by the

423   difference between the intensity (grey level) of certain "features of interest" and the intensity

424 of the "background" within a selected region, divided by the sum of the two intensities. Other

425 possible metrics could be utilized as well, such as the width of the local image histogram, the

426 "universal image quality index" [39] and others.

427

428

429 **5. CONCLUSIONS**

430

431 We have presented the results of PB-CT X-ray phase-contrast imaging of seven full

432 unfixed mastectomy samples performed at Imaging and Medical beamline of the Australian

433 Synchrotron. We have compared the CT reconstructions of the same samples obtained in the

434 conventional absorption-only ("contact") CT regime and in the PB-CT regime at the sample-

435 to-detector distance of 6 m. The radiation dose delivered to the samples during the scans was

436 comparable to that approved for routine mammography or breast tomosynthesis. We have

437 shown that the image quality, as assessed by nine experienced medical imaging specialists

438 and five practicing radiologists was, on average, higher in the PB-CT images compared to

439 absorption-only CT images collected at an equivalent dose. We have argued that further

440 improvement of the X-ray imaging hardware (primarily, the X-ray detector) used in this type

441 of imaging, is expected to bring further substantial gains in the image quality in the PB-CT

442 mode. The assessment results by the imaging experts and radiologists were found to be

443 generally consistent with the objective measurements of SNR and spatial resolution in the

444 reconstructed CT slices of mastectomy samples. These results constitute part of the

445 systematic research that our collaborative team has been conducting with the goal of

446 developing medical breast cancer imaging facilities at the Australian Synchrotron in

447 Melbourne, Australia, and at Elettra Synchrotron in Trieste, Italy [11,15,25,27,40].

448

449

456

457

458   **CONFLICT OF INTEREST**

459

460   The authors have no conflicts to disclose.

461

462

463

464   **REFERENCES**

465

466   1.   Fitzmaurice C, et al. Global, Regional, and National Cancer Incidence, Mortality,
467   Years of Life Lost, Years Lived With Disability, and Disability-Adjusted Life-Years
468   for 29 Cancer Groups,1990 to 2016. A Systematic Analysis for the Global Burden of
469   Disease Study. *JAMA Oncol.* 2018; 4(11):1553-1568.

470   2.   Harvard Medical School. What do the new mammography guidelines mean for you?
471   http://www.health.harvard.edu/womens-health/what-do-the-new-mammography-
472   guidelines-mean-for-you. Accessed May 7, 2019.

473   3.   Keyrilainen J, Bravin A, Fernandez M, Tenhunen M, Virkkunen P and Suortti P.
474   Phase-contrast X-ray imaging of breast. *Acta Radiol.* 2010; 51**:**866-884.

475   4.   Tromba G, Cova MA, Castelli E. Phase-contrast mammography at the SYRMEP
476   beamline of Elettra. *Synchrotron Radiation News.* 2011; 24**:**3-7.

477   5.   Malliori A, Bliznakova K, Speller RD, et al. Image quality evaluation of breast
478   tomosynthesis with synchrotron radiation *Med.Phys.* 2012; 39(9):5621-5634.

479   6.   Zhao Y, Brun E, Coan P, et al. High-resolution, low-dose phase contrast X-ray
480   tomography for 3D diagnosis of human breast cancers. *Proc Natl Acad Sci USA.*
481   2012; 109:18290-18294.

482   7.   Bravin A, Coan P and Suortti P. X-ray phase-contrast imaging: from pre-clinical
483   applications towards clinics. *Phys Med Biol.* 2013; 58:R1-R35.

484   8.   Coan P, Bravin A and Tromba G. Phase-contrast x-ray imaging of the breast: recent
485   developments towards clinics. *Journal of Physics D: Applied Physics.* 2013; 46:
486   494007.

487   9.   Olivo A, Gkoumas S, Endrizzi M, et al. Low-dose phase contrast mammography with
488   conventional x-ray sources. *Med Phys.* 2013; 40:090701.

489   10.   Brun F, Pacilè S, Accardo A, et al. Enhanced and flexible software tools for X-ray
490   computed tomography at the Italian synchrotron radiation facility Elettra.
491   *Fundamenta Informaticae.* 2015; 141:233-243.

492   11.   Pacile S, Brun F, Dullin C, et al. Clinical application of low-dose phase contrast
493   breast CT: methods for the optimization of the reconstruction workflow. *Biomed Opt*
494   *Express.* 2015; 6:3099-3112.

495   12.   Pisano ED, Yaffe MJ. Breast cancer screening: should tomosynthesis replace digital
496   mammography? *JAMA*. 2014; 311(24): 2488-2489.

497   13.   Alakhras MM, Brennan PC, Rickard M, Bourne R, Mello-Thoms C. Effect of
498   radiologists' experience on breast cancer detection and localization using digital breast
499   tomosynthesis. *Europ. Radiol.* 2015; 25(2):402-409.

500   14.   Gureyev T, Mayo S, Nesterets YI, et al. Investigation of the imaging quality of
501   synchrotron-based phase-contrast mammographic tomography *J. Phys. D: Appl. Phys.*
502   2014; 47:365401.

503   15.   Baran PM, Pacile S, Nesterets YI, et al., Optimization of propagation-based x-ray
504   phase-contrast tomography for breast cancer imaging, *Phys.Med.Biol.* 2017;
505   62(6):2315-2332.

506   16.   Kitchen MJ, Buckley GA, Gureyev TE, Wallace MJ, Andres-Thio N, Uesugi K, Yagi
507   N, Hooper SB. CT dose reduction factors in the thousands using X-ray phase contrast,
508   *Scientific Reports.* 2017; 7:15953.

509   17.   Papas MA, Klassen AC. Pain and discomfort associated with mammography among
510   urban low-income African-American women. *J Community Health*. 2005; 30(4):253-
511   267.

512   18.   Miller D, Livingstone V, Herbison P. Interventions for relieving the pain and
513   discomfort of screening mammography. *Cochrane Database Syst Rev.* 2008; Jan
514   23;(1):CD002942 (2008)

515   19.   Boone JM, Nelson TR, Lindfors KK, Seibert JA. Dedicated breast CT: radiation dose
516   and image quality evaluation. *Radiology*. 2001; 221(3):657-667.

517   20.   Pacile S, Baran P, Dullin C. Advantages of breast cancer visualization and
518   characterization using synchrotron radiation phase-contrast tomography. *J. Synch.*
519   *Rad.* 2018; 25:1460-1466.

520   21.   Diemoz PC, Bravin A, Sztrokay-Gaul A, et al. A method for high-energy, low-dose
521   mammography using edge illumination x-ray phase-contrast imaging. *Phys. Med.*
522   *Biol.* 2016; 61:8750–8761.

523   22.   Hellerhoff K, Birnbacher L, Sztrokay-Gaul A, et al. Assessment of intraductal
524   carcinoma in situ (DCIS) using grating-based X-ray phasecontrast CT at conventional
525   X-ray sources: An experimental ex-vivo study. *PLoS ONE*. 2019; 14(1):e0210291.

526 23. Keyrilainen J, Fernández M, Bravin A, et al. Comparison of in vitro breast cancer

527   visibility in analyser-based computed tomography with histopathology,

528   mammography, computed tomography and magnetic resonance imaging. *J. Sync.*

529   *Rad.* 2011; 18(5):689-696.

530 24. Wilkins SW, Gureyev TE, Gao D, Pogany A, Stevenson AW. Phase-contrast imaging

531   using polychromatic hard X-rays. *Nature.* 1996; 384:335-338.

532 25. Taba ST, Baran P, Lewis S, et al. Toward Improving Breast Cancer Imaging:

533   Radiological Assessment of Propagation-Based Phase-Contrast CT Technology.

534   Acad. Radiol. (2018). [published online August 25, 2018]

535 26. Taba ST, Gureyev TE, Alakhras M, Lewis S, Lockie D, Brennan PC. X-ray phase-

536   contrast technology in breast imaging: principles, options, and clinical application,

537   *Am. J. Roentgen.* 2018; 211:133-145.

538 27. Longo R, Tonutti M, Rigon L, et al. Towards breast tomography with synchrotron

539   radiation at Elettra: first images. *Phys Med Biol.* 2016; 61:1634-1649.

540 28. Nesterets YI, Gureyev TE, Mayo SC, et al. A feasibility study of X-ray phase-contrast

541   mammographic tomography at the Imaging and Medical beamline of the Australian

542   Synchrotron *J Synch Rad.* 2015; 22:1509-1523.

543 29. Stevenson AW, Crosbie JC, Hall CJ, Hausermann D, Livingstone J, Lye JE.

544   Quantitative characterization of the X-ray beam at the Australian Synchrotron

545   Imaging and Medical Beamline (IMBL). *J. Synch. Rad.* 2017; 24:110-141.

546 30. Gureyev TE, Baran P, Pacile S., et al. Synchrotron-Based X-ray Phase-Contrast

547   Tomography for Breast Cancer Imaging. *Microsc. Microan.* 2018; 24(S2): 146-147.

548 31. Natterer F. *The Mathematics of Computerized Tomography.* Chichester and New

549   York; John Wiley & Sons; 1986.

550 32. Johns PC, Yaffe MJ. Theoretical optimization of dual-energy x-ray imaging with

551   application to mammography. *Med Phys.* 1985; 12:289-96.

552 33. Paganin D, Mayo SC, Gureyev TE, Miller PR, Wilkins SW. Simultaneous phase and

553   amplitude extraction from a single defocused image of a homogeneous object. *J.*

554   *Microsc.* 2002; 206:33-40.

555 34. Gureyev TE, Nesterets Y, Ternovski D, et al. Toolbox for advanced X-ray image

556   processing. *Proc SPIE .* 2011; 8141:81410B-1.

557 35. Nesterets YI, Gureyev TE. Noise propagation in x-ray phase-contrast imaging and

558   computed tomography. *J Phys D: Appl Phys.* 2014; 47:105402.

36.   Gureyev T, Mohammadi S, Nesterets Y, Dullin C, Tromba G. Accuracy and precision of reconstruction of complex refractive index in near-field single-distance propagation-based phase-contrast tomography. *J Appl Phys.* 2013; 114:144906.

37.   Gureyev TE, Nesterets YI, de Hoog F, et al. Duality between noise and spatial resolution in linear systems. *Opt Express.* 2014; 22:9087-9094.

38.   Gureyev TE, Nesterets YI, Kozlov A, Paganin DM, Quiney HM. On the "unreasonable" effectiveness of Transport of Intensity imaging and optical deconvolution. *J.Opt.Soc.Am. A.* 2017; 34:2251-2260.

39.   Wang Z, Bovik AC. A universal image quality index. *IEEE Signal Proc. Lett.* 2002; 9(3):81–84.

40.   Longo R, Arfelli F, Bonazza D, et al. Advancements towards the implementation of clinical phase-contrast breast computed tomography at Elettra. *J Sync Rad.* 2019; 26: 1343-1353.

Figure legends

Fig. 1. (a) An example of a single X-ray projection of mastectomy sample C4 collected at sample-to-detector distance of 6 m at "low" X-ray dose (2.4 mGy per complete CT scan), and, (b) the corresponding "stitched" full-height projection corrected for dark current and flat field, and for defective pixels.

Fig. 2. Sagittal slice of sample C1 reconstructed from: (a) contact projections, and (b) projections collected at $R = 6$ m, both obtained in CT scans at "std" dose.

Fig. 3. Average imaging experts comparison score (green, triangles), average radiologists comparison score (red, squares) and difference between average SNR/resolution values for the "test" and "reference" images (blue, circles). The data points1 to 14 here are in the same order as in Table 2.

Fig. 4. Axial slice of sample C3 reconstructed from: (a) contact projections at "std" doze, and (b) projections collected at $R = 6$ m at "low" dose. The PB-CT image in (b) was assessed as having higher quality, even though the radiation dose at which it was collected was lower. This sample did not contain any cancerous tumours.

593   Fig. 5. Axial slice of sample C5 reconstructed from: (a) contact projections, and (b)

594   projections collected at $R = 6$ m, both obtained in CT scans at "std" dose. A large tumour is

595   clearly visible in both images. The PB-CT image in (b) was assessed as having higher

596   quality, even though the measured SNR and spatial resolution were apparently better in

597   image (a) (see Table 2).

1   Table 1. Main characteristics of mastectomy samples and imaging parameters used in the present study.

Case No.	Prior treatment	Diagnosis	Weight and size (from pathology reports)	X-ray dose (mGy)
C1		A rare focus of atypical lobular hyperplasia. Fibrocystic changes with epithelial hyperplasia and benign / sclerosing adenosis. Benign fibroadenomata. No DCIS or invasive tumour.	Left breast mastectomy weighing 311g and measuring 160mm from lateral to medial, 120mm from superior to inferior and 25mm from anterior to posterior.	6.0m std = 4.5 6.0m low =2.4 0.2m std = 3.3
C2		Fibrocystic changes with epithelial hyperplasia and benign / sclerosing adenosis. Benign fibroadenomata. No DCIS or invasive tumour.	Right breast skin and nipple sparing mastectomy, weighing 316g and measuring 160mm from medial to lateral, 160mm from superior to inferior, and up to 30mm from anterior to posterior.	6.0m std = 4.3 6.0m low =2.4 0.2m std = 3.2
C3	Wide local excision +/- mammoplasty + sentinel node biopsy. Re-incision of medial margin.	A 2mm focus of high grade DCIS, margins clear. Changes consistent with previous surgery. An additional 3mm focus of high grade DCIS in the lateral half of the scarred area. There is no invasive tumour seen.	Right mastectomy specimen weighing 336g, measuring 150mm from medial to lateral, 115mm from superior to inferior, 50mm from anterior to posterior.	6.0m std = 4.4 6.0m low =2.6 0.2m std = 3.1

C4	Breast core biopsy. Chemotherapy for breast Ca	Invasive carcinoma, NST, BRE Grade 3. Number of tumours - multifocal, multicentric. High grade ductal carcinoma in-situ. Intralymphatic/intravascular tumour present. The maximum dimension of tumour bed - more than 100mm. Invasive tumour dimension - multiple tumour foci 0.5mm to 15mm. Circumferential (radial) margins clear.	Right breast mastectomy specimen, weighing 446g, measuring 170mm from lateral to medial, 150mm from superior to inferior, 35mm from anterior to posterior.	6.0m std = 4.3 6.0m low =2.4 0.2m std = 3.2
C5		One invasive carcinoma, NST, BRE grade 3. In-situ tumour: not seen. Maximum tumour dimension: 35mm. Invasive tumour dimension: 35mm. Intralymphatic / intravascular tumour: present. Fibrocystic change; one benign intramammary node.	Right breast mastectomy specimen, weighing 318g, measuring 170mm medial to lateral, 140mm superior to inferior, 35mm anterior to posterior.	6.0m std = 4.3 6.0m low =2.3 0.7m std = 3.4
C6	Chemotherapy for breast Ca	No evidence of an in-situ or invasive malignancy.	Right breast skin and nipple sparing mastectomy weighing 565g, measuring 190mm medial to lateral, 160mm superior to inferior, 35mm anterior to posterior.	6.0m std = 4.5 6.0m low =2.3 0.7m std = 3.4

| C7 | | Invasive carcinoma (NST), modified Bloom-Richardson-Elston grade 3, with a minor component of intermediate-grade DCIS, 30mm in maximum dimension, no lymphovascular invasion was seen, clear of excision margins. | Right breast mastectomy weighing 617g, measuring 200mm medial to lateral, 120mm superior to inferior, 40mm anterior to posterior. | 6.0m std = 4.5
6.0m low =2.3
0.7m std = 3.4 |

2

3

4 Table 2. Measured spatial resolution, SNR and related image characteristics, alongside the comparison scores

5   averaged across nine medical imaging specialists and five radiologists.

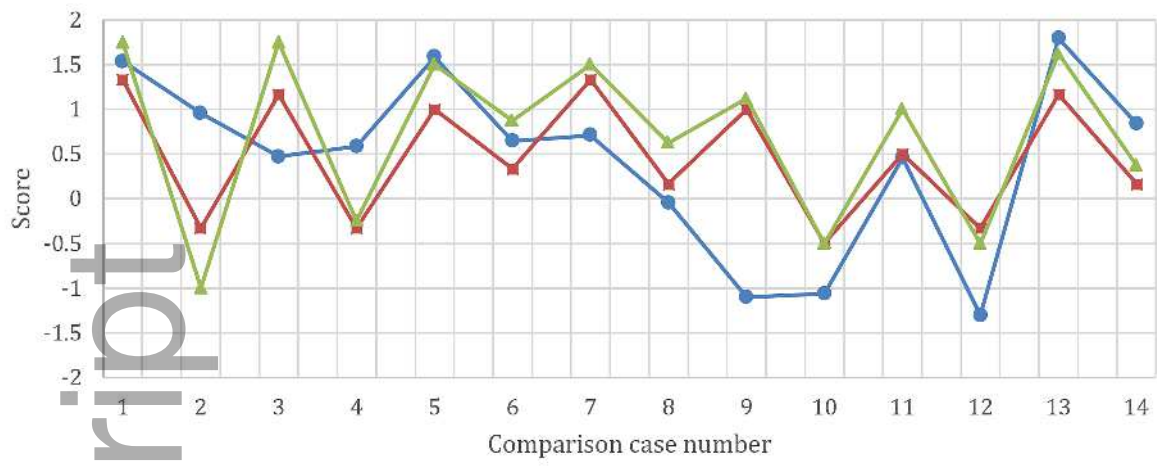| Sample, dose	Ref./test	xres (pix)	yres (pix)	SNR	SNR/res	Δ(SNR/res)	Gain	Experts score	Radiol. score
C1, std	Ref_1	1.93	1.38	5.38	3.30				
1	Test_1	1.96	1.95	9.46	4.84	1.54	1.76	1.75	1.33
C1, low	Ref_10	1.93	1.38	5.22	3.22				
2	Test_10	1.88	1.90	7.88	4.17	0.96	1.51	-1.00	-0.33
C2, std	Ref_3	1.98	1.40	6.07	3.66				
3	Test_3	1.97	2.00	8.12	4.14	0.48	1.34	1.75	1.17
C2, low	Ref_14	1.96	1.38	5.59	3.39				
4	Test_14	1.90	1.89	7.53	3.98	0.59	1.35	-0.25	-0.33
C3, std	Ref_12	1.92	1.39	5.42	3.33				
5	Test_12	1.87	1.95	9.40	4.92	1.59	1.74	1.50	1.00
C3, low	Ref_2	1.92	1.40	6.13	3.74				
6	Test_2	1.82	1.91	8.18	4.39	0.65	1.33	0.88	0.33
C4, std	Ref_7	1.92	1.42	6.13	3.71				
7	Test_7	1.86	2.00	8.49	4.42	0.71	1.38	1.50	1.33
C4, low	Ref_13	1.93	1.41	5.95	3.62				
8	Test_13	1.82	1.92	6.67	3.58	-0.04	1.12	0.62	0.17
C5, std	Ref_9	1.99	1.42	8.97	5.35				
9	Test_9	1.97	2.00	8.49	4.25	-1.10	0.95	1.13	1.00
C5, low	Ref_4	2.01	1.44	8.49	4.98				
10	Test_4	1.96	1.94	7.65	3.91	-1.07	0.90	-0.50	-0.50
C6, std	Ref_5	1.98	1.40	10.01	6.01				
11	Test_5	1.98	2.01	12.83	6.47	0.46	1.28	1.00	0.50
C6, low	Ref_11	1.98	1.40	10.19	6.06				
12	Test_11	1.92	1.93	9.16	4.76	-1.31	0.90	-0.50	-0.33
C7, std	Ref_8	1.97	1.40	6.55	3.94				
13	Test_8	1.98	1.99	11.40	5.73	1.80	1.74	1.63	1.17
C7, low	Ref_6	1.99	1.40	6.66	3.96				
14	Test_6	1.91	1.93	9.16	4.80	0.84	1.38	0.38	0.17

6
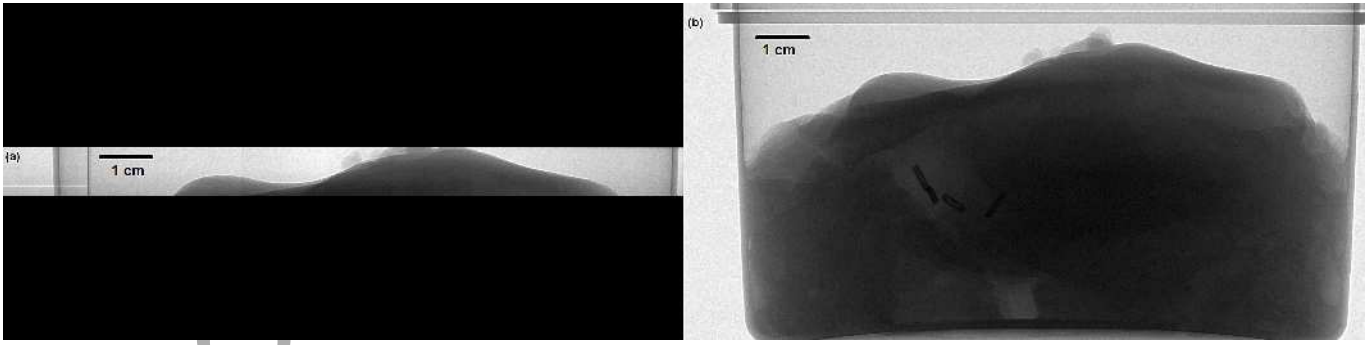
mp_13842_f1.tif
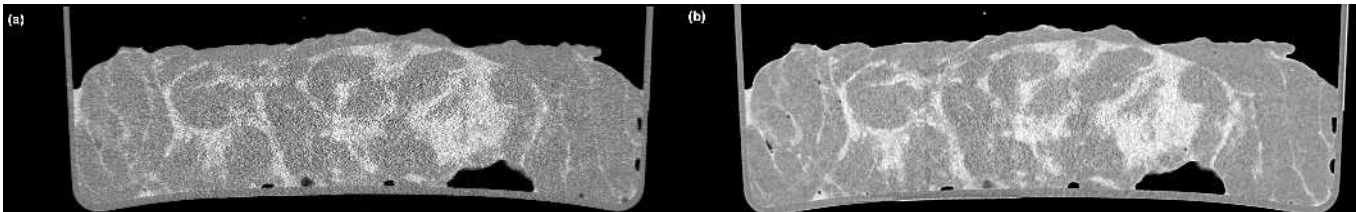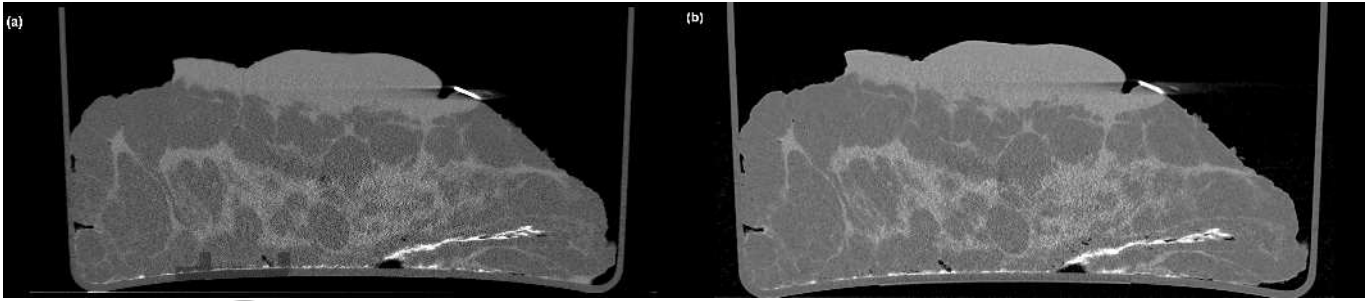
mp_13842_f2.tif

mp_13842_f3.tif

mp_13842_f4.tif
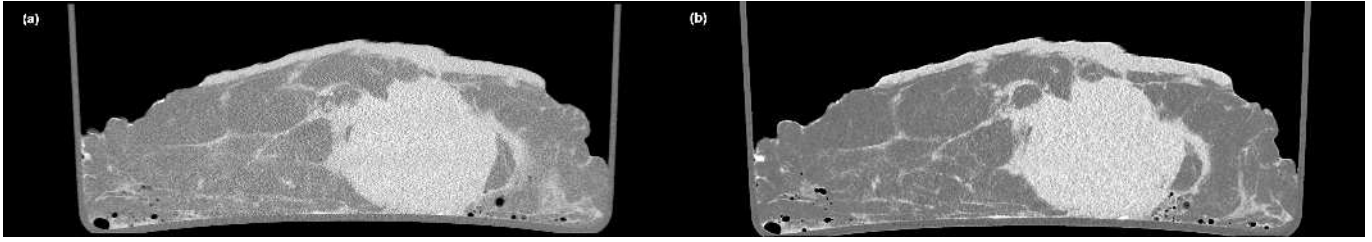
mp_13842_f5.tif

Author/s:

Gureyev, TE;Nesterets, YI;Baran, PM;Taba, ST;Mayo, SC;Thompson, D;Arhatari, B;Mihocic, A;Abbey, B;Lockie, D;Fox, J;Kumar, B;Prodanovic, Z;Hausermann, D;Maksimenko, A;Hall, C;Peele, AG;Dimmock, M;Pavlov, KM;Cholewa, M;Lewis, S;Tromba, G;Quiney, HM;Brennan, PC

Title:

Propagation-based x-ray phase-contrast tomography of mastectomy samples using synchrotron radiation

Date:

2019-10-20